Evaluating the Pharmacokinetics and *In Vivo* Cancer Targeting Capability of Au Nanocages by Positron Emission Tomography Imaging

Yucai Wang,[†,§,⊥] Yongjian Liu,[‡,§,*] Hannah Luehmann,[‡] Xiaohu Xia,[†,⊥] Paige Brown,[†] Chad Jarreau,[‡] Michael Welch,[‡] and Younan Xia[†,⊥,*]

[†]Department of Biomedical Engineering, Washington University, St. Louis, Missouri 63130, United States, and [‡]Department of Radiology, Washington University School of Medicine, St. Louis, Missouri 63110, United States. [§]These authors contributed equally to this work. [⊥]Present address: The Wallace H. Coulter Department of Biomedical Engineering, Georgia Institute of Technology and Emory University, and School of Chemistry and Biochemistry, Georgia Institute of Technology, Atlanta, Georgia 30332.

ABSTRACT

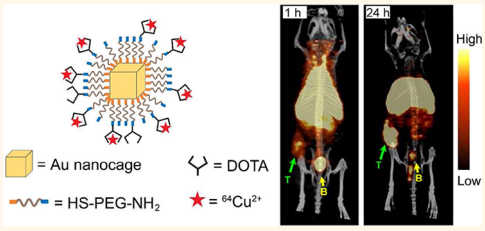

Gold nanocages have recently emerged as a novel class of photothermal transducers and drug carriers for cancer treatment. However, their pharmacokinetics and tumor targeting capability remain largely unexplored due to the lack of an imaging modality for quick and reliable mapping of their distributions *in vivo*. Herein, Au nanocages were prepared with controlled physicochemical properties and radiolabeled with ^{64}Cu in high specific activities for *in vivo* evaluation using positron emission tomography (PET). Our pharmacokinetic studies with femtomolar administrations suggest that 30 nm nanocages had a greatly improved biodistribution profile than 55 nm nanocages, together with higher blood retention and lower hepatic and splenic uptakes. In a murine EMT-6 breast cancer model, the small cages also showed a significantly higher level of tumor uptake and a greater tumor-to-muscle ratio than the large cages. Quantitative PET imaging confirmed rapid accumulation and retention of Au nanocages inside the tumors. The ability to directly and quickly image the distribution of Au nanocages *in vivo* allows us to further optimize their physicochemical properties for a range of theranostic applications.

KEYWORDS: gold nanocage · radiolabeling · positron emission tomography · biodistribution · cancer targeting

Nanomedicine has drawn much attention in recent years because of its great potential in early detection, accurate diagnosis, and personalized therapy of various diseases, especially cancer.[1,2] A rich variety of different nanomaterials, such as polymer nanoparticles, liposomes, and metal nanostructures, have been demonstrated as the platform for a range of applications related to nanomedicine.[3−6] Among them, metal nanostructures, including those based on Au, have received great attention for cancer diagnosis and treatment owing to their bioinertness, easy surface modification, and unique optical properties such as localized surface plasmon resonance (LSPR) and efficient photothermal conversion.[7−9]

As a novel class of nanomaterials, Au nanocages (AuNCs), have recently been explored for cancer imaging and treatment.[10−12] The AuNCs can be easily prepared in large quantities with tunable wall thickness in the range of 2−10 nm through a straightforward, reliable galvanic replacement procedure that involves Ag nanocubes and $HAuCl_4$ in an aqueous solution.[13] By controlling the stoichiometry in a fashion similar to titration, their LSPR peaks can be precisely and reproducibly positioned anywhere in the range of 600−1200 nm, making them ideal candidates as contrast agents for a number of optical imaging modalities.[10,12] Their intrinsic hollow and porous structures can also be used to encapsulate therapeutic payloads for applications related to controlled release or drug delivery.[14,15] Additionally, AuNCs are effective photothermal transducers, capable of converting light into heat and causing the local temperature to rise substantially.[16,17] All of these attributes make AuNCs attractive for an array of theranostic applications.

Despite the successful use of AuNCs in a number of early studies, the pharmacokinetics and *in vivo* tumor targeting capability of AuNCs remain largely unexplored due to the lack of an appropriate imaging modality

* Address correspondence to younan.xia@bme.gatech.edu, liuyo@mir.wustl.edu.

Received for review February 1, 2012 and accepted June 12, 2012.

Published online June 12, 2012
10.1021/nn300464r

for quick, quantitative, and reliable evaluation of their biodistribution. Positron emission tomography (PET), because of its non-invasive, highly sensitive nature, and high patient compliance, has emerged as one of the most frequently used techniques for early stage diagnosis and staging of cancer and other diseases.[18−21] In the past decade, PET imaging in conjunction with well-defined nanostructures has become an increasingly popular tool in various biomedical studies because of the enhanced specificity, sensitivity, and targeting efficiency.[22−26] Here we address the pharmacokinetic and *in vivo* cancer targeting issues of AuNCs by functionalizing their surfaces with radioactive $^{64}Cu^{2+}$ ions for PET imaging. Specifically, AuNCs of two different sizes were prepared, PEGylated, and radiolabeled with $^{64}Cu^{2+}$ ions. We then evaluated the radiolabeling efficiency and *in vivo* pharmacokinetics in normal rodents. In addition, we examined the passive targeting capability of AuNCs *via* the enhanced permeability and retention (EPR) effect in an EMT-6 mouse mammary tumor model by directly imaging with small animal PET/CT.[27] The intratumoral distribution of ^{64}Cu-labeled AuNCs was also examined by autoradiography. This work provides a new platform for further optimization of the physicochemical properties of AuNCs to target a range of theranostic applications.

RESULTS AND DISCUSSION

The main objective of this study is to evaluate the *in vivo* pharmacokinetics and PET imaging capacity of AuNCs with ^{64}Cu radiolabeling so they can be better used in cancer diagnosis and therapy. Nanoparticles with sizes of 10−100 nm are desirable since they may escape from the renal filtering elimination and accumulate at the tumors after prolonged circulation.[28] Moreover, nanoparticles smaller than 60 nm are expected to have better tumor penetration away from blood vessels.[29] Therefore, we prepared AuNCs of 55 and 30 nm in edge length *via* the galvanic replacement reaction between Ag nanocubes of 47 and 25 nm, respectively, in size and aqueous $HAuCl_4$ solution. As shown by the UV−vis spectra in Figure S1 in the Supporting Information, the LSPR peaks of the 55 and 30 nm AuNCs were located at 805 and 760 nm, respectively. Heterofunctional poly(ethylene glycol) (PEG) was then conjugated to the surface of AuNCs through a Au−S linkage to generate PEGylated AuNCs with amine ($-NH_2$) groups on the outer surface. The $-NH_2$ groups were then coupled with 1,4,7,10-tetraazacyclododecane-1,4,7,10-tetraacetic acid mono(*N*-hydroxysuccinimide ester) (DOTA-NHS-ester) through an amide reaction *via* NHS-activated ester, followed by chelating with $^{64}Cu^{2+}$ ions. As shown by the TEM images in Figure 1a,b, the large and small ^{64}Cu-DOTA-PEG-AuNCs had edge lengths of 54.5 ± 4.4 and 30.3 ± 4.2 nm, respectively. Their hydrodynamic diameters were measured to be 96.0 ± 12.0 and 63.7 ± 7.3 nm, respectively, by dynamic light scattering (DLS), together with zeta-potentials (ζ) of 18.7 ± 6.5 and 10.2 ± 1.1 mV (see Table 1). The polydispersity indexes were less than 0.2 for both samples.

To quantify the coverage densities of PEG chains on AuNCs, a fluorescein-tagged PEG-thiol (FITC-PEG-SH, $M_w \approx 5000$) was mixed with NH_2-PEG-SH ($M_w \approx 5000$) at a molar ratio of 1:100 for surface functionalization.[30] After conjugation, AuNCs were completely dissolved in 0.1 M potassium cyanide (KCN) to release the −S-PEG-FITC chains from the metal surface, which would dimerize to form disulfide compounds. The coverage densities of the PEG chains were then quantified using fluorescence spectroscopy with an established calibration curve for FITC-PEG-SH. The average number of PEG chains on each AuNC was found to be approximately 45 000 and 17 000 for the 55 and 30 nm AuNCs, respectively. Therefore, the PEG coverage densities on the surfaces of AuNCs were 1.43 and 1.86 per nm^2 for the 55 and 30 nm AuNCs, respectively. Here the surface area of a AuNC was calculated by including both the outer and inner surfaces, with contributions from the pores being excluded.[30]

The AuNCs were radiolabeled with $^{64}Cu^{2+}$ ions using a procedure previously reported for radiolabeling nanoparticles.[25] Figure 1c shows the typical fast protein liquid chromatography (FPLC) profile of the 30 nm ^{64}Cu-DOTA-PEG-AuNCs traced by both radioactivity and UV detectors. Clearly, the ^{64}Cu-DOTA-PEG-AuNCs could be purified with no aggregation by using centrifugation to remove the remaining free $^{64}Cu^{2+}$ ions.

During the initial exploration of ^{64}Cu radiolabeling of DOTA-PEG-AuNCs, high specific activity could be obtained using the freshly prepared DOTA-PEG-AuNCs. However, during the storage of DOTA-PEG-AuNCs at 4 °C in water, Ag rapidly leached out from the Ag/Au alloy walls of DOTA-PEG-AuNCs and the Ag^+ ion could compete for the DOTA chelator,[31] leading to a significant decrease in the available DOTA for ^{64}Cu radiolabeling and rapid reduction of specific activity in a week. This issue greatly limits the use of AuNCs for PET imaging. To solve this problem, hydrogen peroxide (H_2O_2) was employed as an effective etchant to remove Ag from the surface of AuNCs,[32] which led to a 6.2 ± 0.8% reduction of Ag in the AuNCs as measured by inductively coupled plasma mass spectrometry (ICP-MS, data not shown). As shown in Figure 1d, after treatment with H_2O_2, high specific activity (81.4−107.3 GBq/nmol) of ^{64}Cu radiolabeling was readily achieved for both large and small DOTA-PEG-AuNCs. More importantly, the DOTA-PEG-AuNCs could be stored at 4 °C for a period of time relevant for biological applications while retaining high radiolabeling specific activity, due to the removal of Ag from the surface. Furthermore, our serum stability studies of ^{64}Cu-DOTA-PEG-AuNCs showed that their radiochemical purity only dropped from the original value of >97% to 90.2 ± 0.3% at 4 h and 81.5 ± 1.4% at 24 h, respectively, after incubation

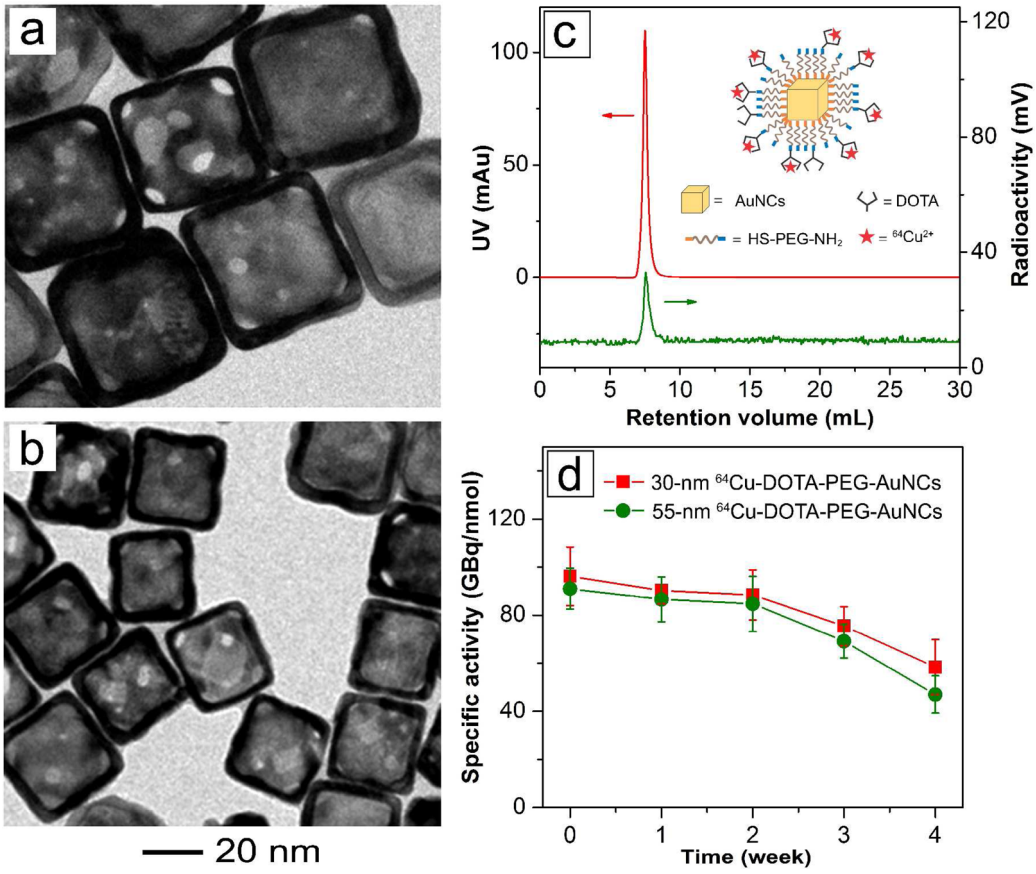

Figure 1. Typical transmission electron microscopy images of DOTA-PEG-AuNCs with an edge length of (a) 54.5 ± 4.4 nm and (b) 30.3 ± 4.2 nm; (c) fast protein liquid chromatography analysis of the 30 nm ^{64}Cu-DOTA-PEG-AuNCs; and (d) longitudinal specific activities of the ^{64}Cu-DOTA-PEG-AuNCs after incubation at 4 °C for different periods of time.

TABLE 1. Summary of the Diameters and Zeta-Potentials of the $^{64}Cu^{2+}$-Labeled PEGylated AuNCs

parameters	large ^{64}Cu-DOTA-PEG-AuNCs	small ^{64}Cu-DOTA-PEG-AuNCs
edge length (nm)[a]	54.5 ± 4.4	30.3 ± 4.2
diameter (nm)[b]	96.0 ± 12.0	63.7 ± 7.3
zeta-potential (mV)[b]	18.7 ± 6.5	10.2 ± 1.1

[a] Determined using transmission electron microscopy (TEM). [b] Determined using dynamic light scattering (DLS).

with mouse serum (10% in PBS) at 37 °C, indicating good stability for the ^{64}Cu-labeled AuNCs. Our previous study demonstrated that AuNCs of 55 nm in size and coated with methoxy-PEG-thiol ($M_w \approx 5000$) could serve as photothermal transducers for effective cancer treatment.[17] However, like other Au nanostructures reported in literature,[33,34] the poor pharmacokinetics resulted in low blood retention and low tumor-to-muscle ratio for the AuNCs,[17] limiting their application as a cancer treatment strategy in translational research. In this study, *in vivo* biodistribution studies of the 55 nm ^{64}Cu-DOTA-PEG-AuNCs showed fast systemic clearance due to high uptakes by the reticuloendothelial system (RES) (liver and spleen) and low blood retention in C57BL/6 mice throughout the study. Liver and spleen uptakes were dominant among all of the organs with more than 60%ID/g at 1 h post-injection. However, the accumulation in liver gradually decreased to 41.6 ± 1.5%ID/g at 24 h, while the uptake by spleen quickly dropped to 7.9 ± 0.4%ID/g (Figure 2a).

For the 30 nm AuNCs, although their photothermal effect was comparable to that of the 55 nm AuNCs when normalized to the number of Au atoms (Figure S2), their biodistributions were found to be considerably different. At 1 h post-injection, the blood retention of the 30 nm ^{64}Cu-DOTA-PEG-AuNCs was 20.6 ± 3.6% ID/g, 6 times greater than what was obtained with the 55 nm ^{64}Cu-DOTA-PEG-AuNCs, and then gradually decreased to 14.6 ± 2.4%ID/g at 4 h and less than 3%ID/g at 24 h. As expected, the liver uptake was the greatest among all of the organs, which remained essentially constant throughout the 24 h period. Similar to the 55 nm AuNCs, the spleen uptake of the 30 nm AuNCs also displayed a fast clearance profile with less than 50% of the initial accumulation remaining at 24 h. Interestingly, kidney levels of the small AuNCs were constant (Figure 2b) during the 24 h of study, while the large AuNCs showed a 3-fold increase of kidney accumulation from 1 to 24 h (Figure 2a). Compared to the 55 nm AuNCs, the 30 nm AuNCs showed much

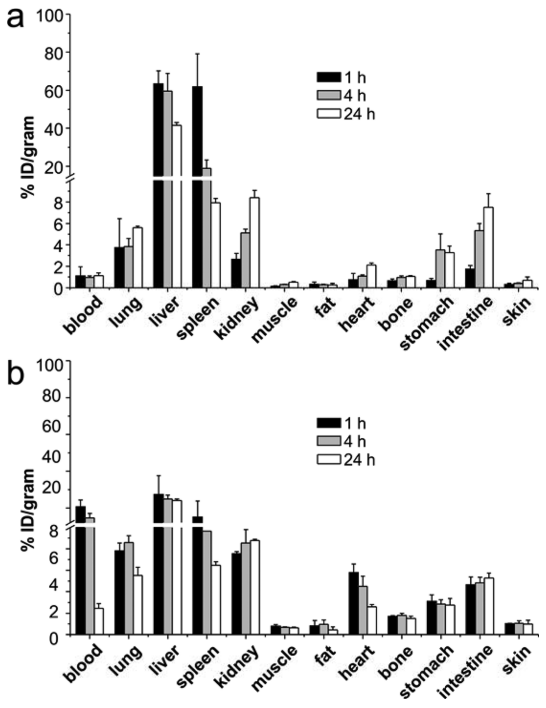

Figure 2. Biodistribution of (a) the large ^{64}Cu-DOTA-PEG-AuNCs (55 nm) and (b) the small ^{64}Cu-DOTA-PEG-AuNCs (30 nm) in C57BL/6 mice (0.37 MBq injection/mouse, n = 4 per group).

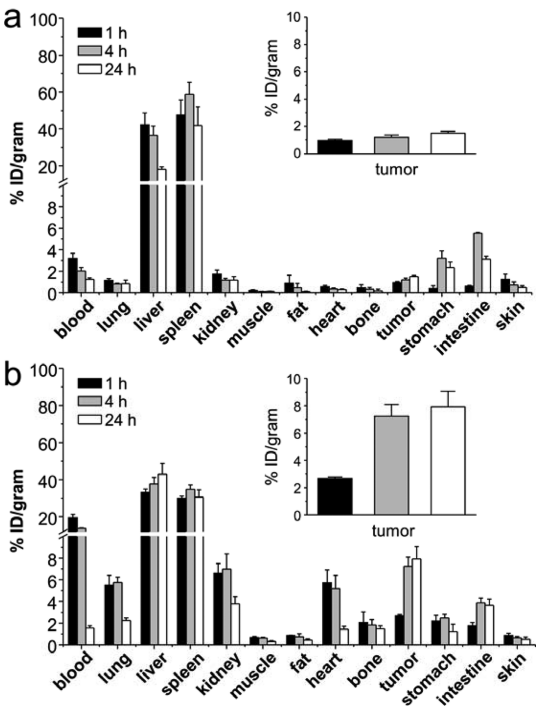

Figure 3. Biodistribution of (a) the large ^{64}Cu-DOTA-PEG-AuNCs (55 nm) and (b) the small ^{64}Cu-DOTA-PEG-AuNCs (30 nm) in EMT-6 tumor-bearing mice (0.37 MBq injection/mouse, n = 4 per group).

improved *in vivo* pharmacokinetics with high retention in blood pool (blood, lung, and heart) and decreased RES uptake, likely due to the reduction in size and surface charge. This trend was consistent with previous reports about the effects of size and surface charge of nanostructures on *in vivo* biodistribution.[34,35]

We next studied the biodistribution of ^{64}Cu-DOTA-PEG-AuNCs in EMT-6 tumor-bearing mice. The accumulation level in tumors depends on factors such as the size of nanoparticles, the blood circulation half-life (a longer half-life leads to higher accumulation), the degree of tumor vascularization (higher accumulation in more vascularized tumors), and the degree of angiogenesis (high accumulation in tumors of rapid and defected angiogenesis). The EMT-6 tumor model was selected for this study because it is known to grow rapidly and featured with tumor angiogenesis, as well as high vessel permeability.[36,37] For the EMT-6 tumor-bearing BALB/c mice, the 55 nm ^{64}Cu-DOTA-PEG-AuNCs showed a distribution pattern similar to what was obtained in normal mice with high hepatic and splenic uptakes. Interestingly, unlike the rapid drop of spleen accumulation observed in C57BL/6 mice, the spleen accumulation of 55 nm ^{64}Cu-DOTA-PEG-AuNCs in EMT-6 tumor-bearing mice was constant up to 24 h, probably due to the difference in animal species. However, tumor uptake of the 55 nm ^{64}Cu-DOTA-PEG-AuNCs was low (together with a slight increase during the 24 h of study) due to their poor retention in blood (Figure 3a). With decrease in muscle uptake, the tumor-to-muscle ratio increased dramatically from 4.13 $\pm$ 0.96 at 1 h to 11.9 $\pm$ 1.72 at 4 h and remained constant afterward (12.8 $\pm$ 4.17 at 24 h). The tumor-to-blood ratio also increased from 0.30 $\pm$ 0.05 at 1 h to 1.20 $\pm$ 0.18 at 24 h.

The 30 nm ^{64}Cu-DOTA-PEG-AuNCs in tumor-bearing mice had a biodistribution profile similar to what was acquired for normal animals with high RES system uptakes. The blood retentions were all significantly ($p < 0.05$, n = 4) higher than those obtained with the 55 nm ^{64}Cu-DOTA-PEG-AuNCs, with about 20%ID/g at the beginning and then rapidly cleared. The initial tumor uptake was 2.68 $\pm$ 0.12%ID/g at 1 h, rapidly increased to 7.2 $\pm$ 0.9%ID/g at 4 h, and then gradually increased to 7.9 $\pm$ 1.1%ID/g at 24 h (Figure 3b), which was more than 4 times higher than what was obtained with the 55 nm ^{64}Cu-DOTA-PEG-AuNCs, likely due to a longer blood circulation time and a better EPR effect. Further, these small AuNCs exhibited a rapid increase and then sustained retention profile for tumor uptake, which is important for a longitudinal and repeated photothermal treatment of cancer. Additionally, owing to the rapid blood clearance, the tumor-to-muscle ratios also rapidly increased to 25.7 $\pm$ 6.9 at 24 h. For tumor-to-blood ratio, it also increased from 0.14 $\pm$ 0.01 at 1 h to 5.15 $\pm$ 1.05 at 24 h. Although the large AuNCs showed comparable contrast ratios at the beginning, the contrast ratio of the small AuNCs at 24 h was twice as much as that of the large AuNCs owing to the higher tumor uptake. It is worth mentioning that extending

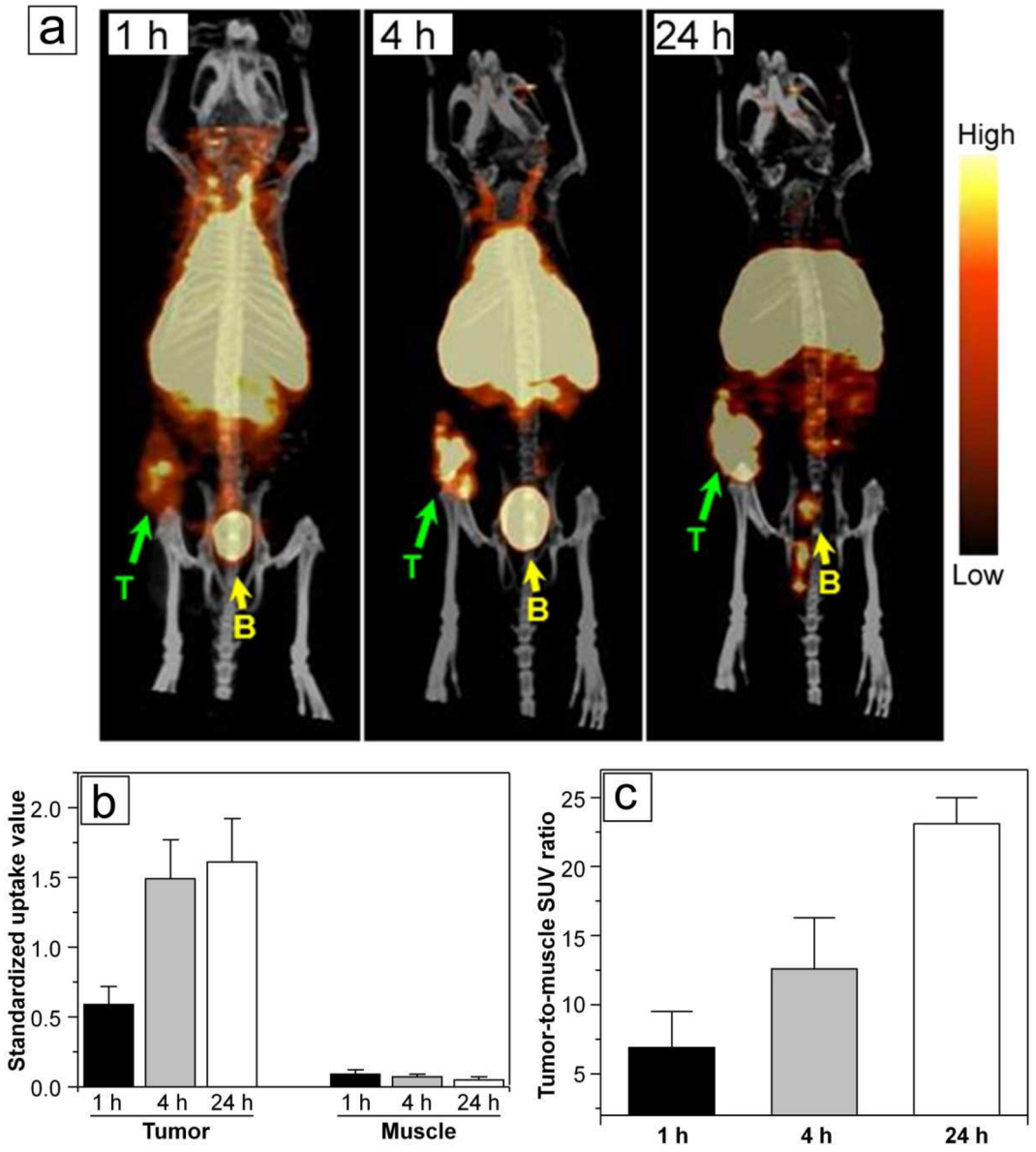

Figure 4. (a) PET/CT images of the 30 nm ^{64}Cu-DOTA-PEG-AuNCs in a mouse bearing an EMT-6 tumor at 1, 4, and 24 h post-injection (3.7 MBq injection/mouse). T, tumor; B, bladder. (b) Standardized uptake values (SUV) in tumor and muscle regions obtained from PET/CT images taken at different times. (c) Tumor-to-muscle SUV ratios obtained from PET/CT images taken at different time points.

the measurement time would increase error due to the low counts since only a trace amount $^{64}Cu^{2+}$ was administrated *in vivo* (73% of the $^{64}Cu^{2+}$ ions had decayed at 24 h), as well as the fact that more $^{64}Cu^{2+}$ could be dissociated from the ^{64}Cu-DOTA-PEG-AuNCs over time (radiochemical purity dropped to 81.5 ± 1.4% at 24 h). In contrast to the *in vivo* applications of other radiolabeled Au nanostructures (*e.g.*, nanoshells and nanorods) in tumor models, the small ^{64}Cu-DOTA-PEG-AuNCs displayed a comparable level of tumor uptake and tumor-to-muscle ratio.[34]

As indicated in Figure 4a, PET/CT images clearly showed rapid localization of the 30 nm ^{64}Cu-DOTA-PEG-AuNCs in tumors at 1 h post-injection even only with the administration of a trace amount (23.8 fmol). A quantitative analysis of the region of interest (ROI) drawn around the tumor showed increased standardized uptake values (SUVs) from 1 to 24 h, consistent with the biodistribution data (Figure 4b). The increase of tumor-to-muscle ratios was calculated to be consistent with the biodistribution data shown in Figure 4c. Interestingly, compared to the other Au nanostructures, the uptake of the small ^{64}Cu-DOTA-PEG-AuNCs was localized at the center of the tumor as shown by the PET/CT image obtained at 1 h post-injection (Figure 4a). The fast increase of SUVs extracted from the centric tumor suggested the potential to quickly concentrate the AuNCs at the center of a tumor for effective photothermal therapy (Figure 4b).

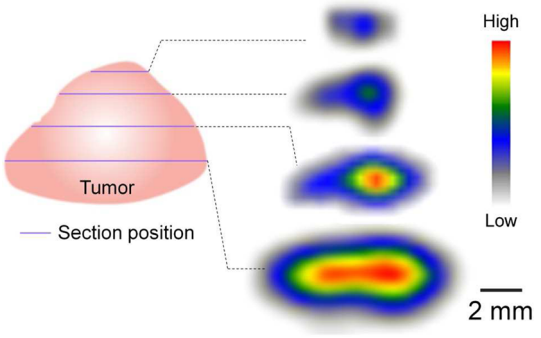

Figure 5. Tumor autoradiography revealing centralized intratumoral accumulation of the 30 nm ^{64}Cu-DOTA-PEG-AuNCs (3.7 MBq injection/mouse) in a mouse bearing an EMT-6 tumor. The tumor was resected at different depth from surface to core region and sectioned into slices of 40 μm thick at 24 h post-injection.

To confirm the intratumoral distribution profile, the EMT-6 tumor was sectioned into 40 μm slices at 24 h post-injection for autoradiographic analysis. The collected tumor images, depicted in Figure 5, clearly showed accumulation of the small ^{64}Cu-DOTA-PEG-AuNCs in the central region of the tumor. For anticancer therapeutic intratumoral delivery, a major challenge is that the drug is limited to the periphery of the tumor mass close to the vasculature due to the physiological barriers presented by the abnormal tumor vasculature and interstitial matrix.[38−40] As such, the central region of a tumor might remain untouched, becoming a potential source for cancer relapse or metastasis.[41] Besides the enhanced EPR effect in the tumor, the main mechanism for transporting nanoparticles intratumorally is diffusion, which is largely affected by the size, surface charge, and morphology, as well as the physicochemical properties of the interstitial matrix.[42] Previously, we found that the 55 nm AuNCs, following tail vein injection, were more abundant at the host interface rather than the central region. Here, due to the small size and nearly neutral charge of the 30 nm ^{64}Cu-DOTA-PEG-AuNCs,[43] a uniform blood flow of the EMT-6 tumor,[40] and possibly a low interstitial pressure in the tumor,[44] the small AuNCs displayed a centralized localization in the EMT-6 tumor, which may reduce its extravasation into the surrounding tissue during photothermal treatment and improve the therapeutic efficacy.[45] Further, the quantitative SUV analysis showed high contrast ratios of tumor uptake to the surrounding tissue, consistent with the biodistribution results. Combined with their good biocompatibility (Figure S3), especially upon PEGylation, the ^{64}Cu-labeled AuNCs show great promise for tracking their *in vivo* fates by PET imaging.

CONCLUSION

We have demonstrated the modular construction of differently sized AuNCs (55 and 30 nm) with tailored physiochemical properties, *in vivo* pharmacokinetics evaluation, and PET imaging of ^{64}Cu-labeled DOTA-PEG-AuNCs in an EMT-6 murine mammary carcinoma model. Both the large and small ^{64}Cu-DOTA-PEG-AuNCs had high radiolabeling specific activities and stabilities. The 30 nm ^{64}Cu-DOTA-PEG-AuNCs showed much improved *in vivo* pharmacokinetics with decreased RES system uptake and enhanced blood circulation compared to the 55 nm samples. The PET/CT imaging demonstrated rapid accumulation and centralized distribution of the 30 nm ^{64}Cu-DOTA-PEG-AuNCs in tumors and, more importantly, high tumor-to-muscle ratios. These results suggest the use of PET imaging as a powerful tool for optimizing the great potential of AuNCs as a theranostic agent for cancer research.

MATERIALS AND METHODS

Chemicals. Amine polyethylene glycol thiol (NH_2-PEG-SH, $M_w \approx 5000$) was purchased from Laysan (Arab, AL). Fluorescein-tagged polyethylene glycol thiol (FITC-PEG-SH, $M_w \approx 5000$) was obtained from Nanocs (Boston, MA). 1,4,7,10-Tetraazacyclododecane-1,4,7,10-tetraacetic acid mono(*N*-hydroxysuccinimide ester) (DOTA-NHS-ester) was purchased from Macrocyclics (Dallas, TX) and used as received. All other chemicals were obtained from Sigma-Aldrich (St. Louis, MO).

Preparation, Functionalization, and Characterization of AuNCs. AuNCs with two different sizes (55 and 30 nm in edge length) covered with poly(vinyl pyrrolidone) were prepared using a galvanic replacement reaction between Ag nanocubes (47 and 25 nm in edge length, respectively) and chloroauric acid following the previously reported protocol.[46] The reaction was monitored by measuring the localized surface plasmon resonance (LSPR) peaks with UV−vis spectroscopy (Cary 50 spectrometer, Varian, Palo Alto, CA) during the reaction. The LSPR was tuned to ~800 nm for 55 nm AuNCs, while 30 nm AuNCs were obtained at ~760 nm.

Both AuNCs were first functionalized with NH_2-PEG-SH and then conjugated with DOTA-NHS-ester for ^{64}Cu radiolabeling. Briefly, 5.0 mL of 2 nM AuNCs in ultrapurified water (Millipre, Billerica, MA) was added to 5.0 mg of NH_2-PEG-SH (PEG/AuNC = 10^5:1) and reacted overnight at 4 °C under stirring. The excess NH_2-PEG-SH was removed by centrifugation at 12 000 rpm for 8 min and washed five times with ultrapurified water to obtain PEGylated AuNCs. The PEGylated AuNCs were reconstituted in 0.1 M (pH 7.4) phosphate buffer prechelexed to remove any trace metal. The solution was mixed with 9.5 mg of DOTA-NHS-ester (DOTA/AuNC = 10^6:1) and reacted at 20 °C for 1 h followed by thorough centrifugation at 12 000 rpm for 8 min and washing with ultrapurified water to remove the unconjugated DOTA-NHS-ester and to obtain DOTA-PEG-AuNCs.

The samples were examined using a Tecnai G2 Spirit transmission electron microscope (TEM) operated at 120 kV (FEI, Hillsboro, OR). Dynamic light scattering (NanoZS, Malvern, Worcestershire, UK) was performed to measure the hydrodynamic diameter, zeta-potential, and polydispersity index of these samples.

Quantification of PEGylation Density. To measure the PEGylation density, FITC-PEG-SH ($M_w \approx 5000$) was mixed with NH_2-PEG-SH ($M_w \approx 5000$) at a 1:100 molar ratio for surface conjugation. After reaction overnight at 4 °C, the excess NH_2-PEG-SH was removed by centrifugation at 12 000 rpm for 8 min and washed five times with ultrapurified water. The FITC-labeled PEGylated AuNCs

were completely dissolved in 0.1 M potassium cyanide (KCN). The fluorescence signal was measured with excitation at 488 nm and emission collection at 520 nm. The quantification of AuNCs' PEGylation density was calculated from a calibration curve established from FITC-PEG-SH.

^{64}Cu Radiolabeling and Stability. Copper-64 ($t_{1/2}$ = 12.7 h, β^+ = 17%, β^- = 40%) was produced on the Washington University Medical School CS-15 cyclotron by the ^{64}Ni (p,n) ^{64}Cu nuclear reaction at a specific activity of 1.85−7.40 GBq/μg at the end of bombardment.[47] DOTA-PEG-AuNCs (about 0.1 pmol) were incubated with 185 MBq ^{64}Cu in 0.1 M sodium acetate buffer (pH 7.0) at 55 °C for 1 h to get the maximal labeling specific activity. After ethylene diamine tetraacetic acid (EDTA, 10 mM in 50 mM pH 7.4 phosphate buffer) challenge, the ^{64}Cu-labeled DOTA-PEG-AuNCs were purified by ultracentrifugation at 12 000 rpm for 8 min for five times. The radiochemical purity of ^{64}Cu-DOTA-PEG-AuNCs was monitored by radio instant thin layer chromatography (radio-ITLC, Bioscan, Washington, DC). DOTA-PEG-AuNCs were labeled with nonradioactive $CuCl_2$ following the same labeling and purification procedures as ^{64}Cu.

To minimize the interference of Ag ions leached from the AuNCs during ^{64}Cu radiolabeling, hydrogen peroxide was used to pretreat the AuNCs prior to PEGylation and DOTA functionalization.[32] The concentrations of Au and Ag in AuNCs were measured by Elan DRC II inductively coupled plasma mass spectrometry (ICP-MS, Perkin-Elmer, Waltham, MA). Briefly, 10 μL of AuNC aqueous suspensions was completely digested with 8 mL of aqua regia (HCl/HNO_3 = 3:1 (v/v)) in a 100 mL beaker at 130 °C. The solution was evaporated to 5 mL and subsequently diluted to 12 mL using 0.5% HCl and 2% HNO_3. Quantification was carried out by external five-point calibration with internal standard correction.

The long-term radiolabeling stability of ^{64}Cu-DOTA-PEG-AuNCs was tested in ultrapurified water at 4 °C over a one month period. The serum stability of ^{64}Cu-DOTA-PEG-AuNCs was also assessed by incubation with mouse serum at 37 °C over a 24 h period. The radiochemical purity and chemical purity of the ^{64}Cu radiolabeled AuNC were measured by AKTA fast protein liquid chromatography system (FPLC) equipped with both radioisotope detector (Beckman 170, Beckman, Brea, CA) and UV detectors (GE Healthcare, Bucks, UK). The AuNC separation was performed on a Superpose 12 10/300 GL size exclusion column (GE Healthcare, Bucks, UK) eluted with 20 mM *N*-(2-hydroxyethyl)piperazine-*N*9-(2-ethanesulfonic acid) (HEPES) and 150 mM NaCl (pH 7.3) with a flow rate of 0.8 mL/min. The UV detector was set at 254 nm.

Animal Biodistribution Studies. All animal studies were performed in compliance with guidelines set forth by the NIH Office of Laboratory Animal Welfare and approved by the Washington University Animal Studies Committee. Biodistribution studies were performed in male C57BL/6 mice weighing 20−25 g (n = 4, Charles River Laboratory, Wilmington, MA), and about 0.37 MBq (2.38 fmol) of ^{64}Cu-DOTA-PEG-AuNCs in 100 μL of saline (APP Pharmaceuticals, Schaumburg, IL) was injected *via* the tail vein. The mice were anesthetized with inhaled isoflurane and reanesthetized before euthanizing them by cervical dislocation at each time point (1, 4, and 24 h post-injection). Organs of interest were collected, weighed, and counted in a well Beckman 8000 gamma counter (Beckman, Brea, CA). Standards were prepared and measured along with the samples to calculate the percentage of the injected dose per gram of tissue (%ID/g).[48]

The EMT-6 murine mammary carcinoma cells were cultured in Waymouth's MB 752/1 medium with 85% 2 mM L-glutamine and 15% fetal bovine serum at 37 °C with 5% CO_2. BALB/c nude mice weighing 20−30 g (Charles River Laboratory, Wilmington, MA) were subcutaneously implanted with 6 × 10^5 EMT-6 cells into the hind flank. The tumors were allowed 10 days (tumor approximately 0.3−0.4 g) of growth before beginning the biodistribution study. The biodistribution studies of ^{64}Cu-DOTA-PEG-AuNCs in EMT-6 tumor-bearing mice (n = 4, 0.37 MBq injection/mouse) were carried out following the same procedures with that in C57BL/6 mice.

PET/CT Imaging. Ten days after the EMT-6 murine mammary carcinoma cells were implanted, mice were anesthetized with isoflurane and injected with 3.7 MBq (23.8 fmol) of ^{64}Cu-DOTA-PEG-AuNCs in 100 μL of saline *via* the tail vein. MicroPET scans were performed on either microPET Focus 220 (Siemens, Malvern, PA) or Inveon PET/CT system (Siemens, Malvern, PA) at 1 h (15 min frame), 4 h (20 min frame), and 24 h post-injection (30 min frame). The microPET images were corrected for attenuation, scatter, normalization, and camera dead time and co-registered with microCT images. All of the PET scanners were cross-calibrated periodically. The microPET images were reconstructed with the maximum a posteriori (MAP) algorithm and analyzed by ASIPro.[49] The tumor uptake of ^{64}Cu-DOTA-PEG-AuNCs was calculated in terms of the standardized uptake value (SUV) in three-dimensional regions of interest (ROIs). In general, SUV is defined as the tissue concentration of radiotracer divided by the activity injected per body weight and is calculated according to the following equation. All the SUV data were not corrected for partial volume effect.[50]

$$\mathrm{SUV} = \frac{\text{radioactivity concentration in ROI}[\mu\mathrm{Ci/mL}]}{\text{injected}\dfrac{\text{dose}[\mu\mathrm{Ci}]}{\text{animal weight}[\mathrm{g}]}}$$

Autoradiography Studies. Digital autoradiographs defining the intratumoral distribution of ^{64}Cu-DOTA-PEG-AuNCs were collected with Canberra Packard Instant Imager (Canberra, Meriden, CT) in a 60 min acquisition period shortly after the tumor was sectioned at 24 h post-injection.

Conflict of Interest: The authors declare no competing financial interest.

Acknowledgment. We thank T. Sharp, N. Fettig, M. Morris, A. Roth, L. Strong, and A. Stroncek for their assistance with animal and imaging studies; T. Voller, E. Madrid, P. Eisenbies, and C. Carey for ^{64}Cu production. This work was supported in part by National Cancer Institute (1R01CA138527-01A1) and start-up funds from Washington University in St. Louis.

Supporting Information Available: UV−vis spectra of AuNCs aqueous suspensions; *in vitro* photothermal study; *in vitro* cell growth inhibition study. This material is available free of charge *via* the Internet at http://pubs.acs.org.

REFERENCES AND NOTES

1. Petros, R. A.; DeSimone, J. M. Strategies in the Design of Nanoparticles for Therapeutic Applications. *Nat. Rev. Drug Discovery* **2010**, *9*, 615–627.
2. Xie, J.; Lee, S.; Chen, X. Y. Nanoparticle-Based Theranostic Agents. *Adv. Drug Delivery Rev.* **2010**, *62*, 1064–1079.
3. Ng, K. K.; Lovell, J. F.; Zheng, G. Lipoprotein-Inspired Nanoparticles for Cancer Theranostics. *Acc. Chem. Res.* **2011**, *44*, 1105–1113.
4. Yoo, D.; Lee, J. H.; Shin, T. H.; Cheon, J. Theranostic Magnetic Nanoparticles. *Acc. Chem. Res.* **2011**, *44*, 863–874.
5. Zrazhevskiy, P.; Gao, X. H. Multifunctional Quantum Dots for Personalized Medicine. *Nano Today* **2009**, *4*, 414–428.
6. Lammers, T.; Aime, S.; Hennink, W. E.; Storm, G.; Kiessling, F. Theranostic Nanomedicine. *Acc. Chem. Res.* **2011**, *44*, 1029–1038.
7. Eustis, S.; El-Sayed, M. A. Why Gold Nanoparticles Are More Precious Than Pretty Gold: Noble Metal Surface Plasmon Resonance and Its Enhancement of the Radiative and Nonradiative Properties of Nanocrystals of Different Shapes. *Chem. Soc. Rev.* **2006**, *35*, 209–217.
8. Erathodiyil, N.; Ying, J. Y. Functionalization of Inorganic Nanoparticles for Bioimaging Applications. *Acc. Chem. Res.* **2011**, *44*, 925–935.
9. Giljohann, D. A.; Seferos, D. S.; Daniel, W. L.; Massich, M. D.; Patel, P. C.; Mirkin, C. A. Gold Nanoparticles for Biology and Medicine. *Angew. Chem., Int. Ed.* **2010**, *49*, 3280–3294.
10. Xia, Y.; Li, W.; Cobley, C. M.; Chen, J.; Xia, X.; Zhang, Q.; Yang, M.; Cho, E. C.; Brown, P. K. Gold Nanocages: From Synthesis to Theranostic Applications. *Acc. Chem. Res.* **2011**, *44*, 914–924.
11. Kim, C.; Cho, E. C.; Chen, J.; Song, K. H.; Au, L.; Favazza, C.; Zhang, Q.; Cobley, C. M.; Gao, F.; Xia, Y.; *et al. In Vivo*

Molecular Photoacoustic Tomography of Melanomas Targeted by Bioconjugated Gold Nanocages. *ACS Nano* **2010**, *4*, 4559–4564.
12. Cai, X.; Li, W.; Kim, C. H.; Yuan, Y.; Wang, L. V.; Xia, Y. *In Vivo* Quantitative Evaluation of the Transport Kinetics of Gold Nanocages in a Lymphatic System by Noninvasive Photoacoustic Tomography. *ACS Nano* **2011**, *5*, 9658–9667.
13. Sun, Y.; Xia, Y. Mechanistic Study on the Replacement Reaction between Silver Nanostructures and Chloroauric Acid in Aqueous Medium. *J. Am. Chem. Soc.* **2004**, *126*, 3892–3901.
14. Moon, G. D.; Choi, S. W.; Cai, X.; Li, W.; Cho, E. C.; Jeong, U.; Wang, L. V.; Xia, Y. A New Theranostic System Based on Gold Nanocages and Phase-Change Materials with Unique Features for Photoacoustic Imaging and Controlled Release. *J. Am. Chem. Soc.* **2011**, *133*, 4762–4765.
15. Yavuz, M. S.; Cheng, Y.; Chen, J.; Cobley, C. M.; Zhang, Q.; Rycenga, M.; Xie, J.; Kim, C.; Song, K. H.; Schwartz, A. G.; *et al.* Gold Nanocages Covered by Smart Polymers for Controlled Release with Near-Infrared Light. *Nat. Mater.* **2009**, *8*, 935–939.
16. Chen, J.; Wang, D.; Xi, J.; Au, L.; Siekkinen, A.; Warsen, A.; Li, Z. Y.; Zhang, H.; Xia, Y.; Li, X. Immuno Gold Nanocages with Tailored Optical Properties for Targeted Photothermal Destruction of Cancer Cells. *Nano Lett.* **2007**, *7*, 1318–1322.
17. Chen, J.; Glaus, C.; Laforest, R.; Zhang, Q.; Yang, M.; Gidding, M.; Welch, M. J.; Xia, Y. Gold Nanocages as Photothermal Transducers for Cancer Treatment. *Small* **2010**, *6*, 811–817.
18. Morrison, A. R.; Sinusas, A. J. Advances in Radionuclide Molecular Imaging in Myocardial Biology. *J. Nucl. Cardiol.* **2010**, *17*, 116–134.
19. Ametamey, S. M.; Honer, M.; Schubiger, P. A. Molecular Imaging with PET. *Chem. Rev.* **2008**, *108*, 1501–1516.
20. Blodgett, T. M.; Meltzer, C. C.; Townsend, D. W. PET/CT: Form and Function. *Radiology* **2007**, *242*, 360–385.
21. Nielsen, C. H.; Kimura, R. H.; Withofs, N.; Tran, P. T.; Miao, Z.; Cochran, J. R.; Cheng, Z.; Felsher, D.; Kjaer, A.; Willmann, J. K.; *et al.* PET Imaging of Tumor Neovascularization in a Transgenic Mouse Model with a Novel ^{64}Cu-DOTA-Knottin Peptide. *Cancer Res.* **2010**, *70*, 9022–9030.
22. Shokeen, M.; Pressly, E. D.; Hagooly, A.; Zheleznyak, A.; Ramos, N.; Fiamengo, A. L.; Welch, M. J.; Hawker, C. J.; Anderson, C. J. Evaluation of Multivalent, Functional Polymeric Nanoparticles for Imaging Applications. *ACS Nano* **2011**, *5*, 738–747.
23. Cai, W. B.; Chen, K.; Li, Z. B.; Gambhir, S. S.; Chen, X. Y. Dual-Function Probe for PET and Near-Infrared Fluorescence Imaging of Tumor Vasculature. *J. Nucl. Med.* **2007**, *48*, 1862–1870.
24. Welch, M. J.; Hawker, C. J.; Wooley, K. L. The Advantages of Nanoparticles for PET. *J. Nucl. Med.* **2009**, *50*, 1743–1746.
25. Liu, Y.; Pressly, E. D.; Abendschein, D. R.; Hawker, C. J.; Woodard, G. E.; Woodard, P. K.; Welch, M. J. Targeting Angiogenesis Using a C-Type Atrial Natriuretic Factor-Conjugated Nanoprobe and PET. *J. Nucl. Med.* **2011**, *52*, 1956–1963.
26. Cheon, J.; Lee, J. H. Synergistically Integrated Nanoparticles as Multimodal Probes for Nanobiotechnology. *Acc. Chem. Res.* **2008**, *41*, 1630–1640.
27. Vavere, A. L.; Welch, M. J. Preparation, Biodistribution, and Small Animal PET of ^{45}Ti-Transferrin. *J. Nucl. Med.* **2005**, *46*, 683–690.
28. Rao, J. H. Shedding Light on Tumors Using Nanoparticles. *ACS Nano* **2008**, *2*, 1984–1986.
29. Popovic, Z.; Liu, W. H.; Chauhan, V. P.; Lee, J.; Wong, C.; Greytak, A. B.; Insin, N.; Nocera, D. G.; Fukumura, D.; Jain, R. K.; *et al.* A Nanoparticle Size Series for *In Vivo* Fluorescence Imaging. *Angew. Chem., Int. Ed.* **2010**, *49*, 8649–8652.
30. Xia, X.; Yang, M; Wang, Y; Zheng, Y.; Li, Q.; Chen, J.; Xia, Y. Quantifying the Coverage Density of Poly(ethylene glycol) Chains on the Surface of Gold Nanostructures. *ACS Nano* **2012**, *6*, 512–522.
31. Kodama, M.; Mahatma, A. B.; Koike, T.; Kimura, E. The Electrochemical Study of Ag(II) Complexes of Polyaza Macrocycles and Their Acetic Acid Derivatives. *Bull. Chem. Soc. Jpn.* **1990**, *63*, 2803–2808.
32. Zhang, Q.; Cobley, C. M.; Zeng, J.; Wen, L. P.; Chen, J.; Xia, Y. Dissolving Ag from Au–Ag Alloy Nanoboxes with H_2O_2: A Method for Both Tailoring the Optical Properties and Measuring the H_2O_2 Concentration. *J. Phys. Chem. C* **2010**, *114*, 6396–6400.
33. Lipka, J.; Semmler-Behnke, M.; Sperling, R. A.; Wenk, A.; Takenaka, S.; Schleh, C.; Kissel, T.; Parak, W. J.; Kreyling, W. G. Biodistribution of PEG-Modified Gold Nanoparticles Following Intratracheal Instillation and Intravenous Injection. *Biomaterials* **2010**, *31*, 6574–6581.
34. Xie, H.; Wang, Z. J.; Bao, A.; Goins, B.; Phillips, W. T. *In Vivo* PET Imaging and Biodistribution of Radiolabeled Gold Nanoshells in Rats with Tumor Xenografts. *Int. J. Pharm.* **2010**, *395*, 324–330.
35. Schipper, M. L.; Iyer, G.; Koh, A. L.; Cheng, Z.; Ebenstein, Y.; Aharoni, A.; Keren, S.; Bentolila, L. A.; Li, J.; Rao, J.; *et al.* Particle Size, Surface Coating, and PEGylation Influence the Biodistribution of Quantum Dots in Living Mice. *Small* **2009**, *5*, 126–134.
36. McQuade, P.; Knight, L. C.; Welch, M. J. Evaluation of ^{64}Cu- and ^{125}I-Radiolabeled Bitistatin as Potential Agents for Targeting $\alpha_v\beta_3$ Integrins in Tumor Angiogenesis. *Bioconjugate Chem.* **2004**, *15*, 988–996.
37. Roberts, W. G.; Hasan, T. Tumor-Secreted Vascular-Permeability Factor Vascular Endothelial Growth-Factor Influences Photosensitizer Uptake. *Cancer Res.* **1993**, *53*, 153–157.
38. Obata, A.; Yoshimoto, M.; Kasamatsu, S.; Naiki, H.; Takamatsu, S.; Kashikura, K.; Furukawa, T.; Lewis, J. S.; Welch, M. J.; Saji, H.; *et al.* Intra-Tumoral Distribution of ^{64}Cu-ATSM: A Comparison Study with FDG. *Nucl. Med. Biol.* **2003**, *30*, 529–534.
39. Minchinton, A. I.; Tannock, I. F. Drug Penetration in Solid Tumours. *Nat. Rev. Cancer* **2006**, *6*, 583–592.
40. Lewis, J. S.; McCarthy, D. W.; McCarthy, T. J.; Fujibayashi, Y.; Welch, M. J. Evaluation of ^{64}Cu-ATSM *in Vitro* and *in Vivo* in a Hypoxic Tumor Model. *J. Nucl. Med.* **1999**, *40*, 177–183.
41. Holback, H.; Yeo, Y. Intratumoral Drug Delivery with Nanoparticulate Carriers. *Pharm. Res.* **2011**, *28*, 1819–1830.
42. Jain, R. K. Transport of Molecules, Particles, and Cells in Solid Tumors. *Annu. Rev. Biomed. Eng.* **1999**, *1*, 241–263.
43. Pluen, A.; Boucher, Y.; Ramanujan, S.; McKee, T. D.; Gohongi, T.; di Tomaso, E.; Brown, E. B.; Izumi, Y.; Campbell, R. B.; Berk, D. A.; *et al.* Role of Tumor–Host Interactions in Interstitial Diffusion of Macromolecules: Cranial *vs.* Subcutaneous Tumors. *Proc. Natl. Acad. Sci. U.S.A.* **2001**, *98*, 4628–4633.
44. Schadlich, A.; Caysa, H.; Mueller, T.; Tenambergen, F.; Rose, C.; Gopferich, A.; Kuntsche, J.; Mader, K. Tumor Accumulation of NIR Fluorescent PEG-PLA Nanoparticles: Impact of Particle Size and Human Xenograft Tumor Model. *ACS Nano* **2011**, *5*, 8710–8720.
45. Kong, G.; Braun, R. D.; Dewhirst, M. W. Characterization of the Effect of Hyperthermia on Nanoparticle Extravasation from Tumor Vasculature. *Cancer Res.* **2001**, *61*, 3027–3032.
46. Skrabalak, S. E.; Au, L.; Li, X.; Xia, Y. Facile Synthesis of Ag Nanocubes and Au Nanocages. *Nat. Protoc.* **2007**, *2*, 2182–2190.
47. McCarthy, D. W.; Shefer, R. E.; Klinkowstein, R. E.; Bass, L. A.; Margeneau, W. H.; Cutler, C. S.; Anderson, C. J.; Welch, M. J. Efficient Production of High Specific Activity ^{64}Cu Using a Biomedical Cyclotron. *Nucl. Med. Biol.* **1997**, *24*, 35–43.
48. Liu, Y.; Ibricevic, A.; Cohen, J. A.; Cohen, J. L.; Gunsten, S. P.; Frechet, J. M.; Walter, M. J.; Welch, M. J.; Brody, S. L. Impact of Hydrogel Nanoparticle Size and Functionalization on *In Vivo* Behavior for Lung Imaging and Therapeutics. *Mol. Pharmaceutics* **2009**, *6*, 1891–1902.
49. Almutairi, A.; Rossin, R.; Shokeen, M.; Hagooly, A.; Ananth, A.; Capoccia, B.; Guillaudeu, S.; Abendschein, D.; Anderson, C. J.; Welch, M. J.; *et al.* Biodegradable Dendritic Positron-Emitting Nanoprobes for the Noninvasive Imaging of

Angiogenesis. *Proc. Natl. Acad. Sci. U.S.A.* **2009**, *106*, 685–690.
50. Liu, Y.; Abendschein, D.; Woodard, G. E.; Rossin, R.; McCommis, K.; Zheng, J.; Welch, M. J.; Woodard, P. K. Molecular Imaging of Atherosclerotic Plaque with ^{64}Cu-Labeled Natriuretic Peptide and PET. *J. Nucl. Med.* **2010**, *51*, 85–91.